

Vignetting Effects: a Tool to Characterize a Fourier Ptychographic Microscope

JOHN MESHREKI^{1,*}, SYED MUHAMMAD KAZIM¹, JAN PHILIPP SCHNEIDER¹, MICHAEL MOELLER¹, AND IVO IHRKE¹

¹University of Siegen, Germany.

*john.meshreki@uni-siegen.de

Compiled April 18, 2024

Fourier Ptychographic Microscopy (FPM) is a recent technique to overcome the diffraction limit of a low numerical aperture (NA) objective lens by algorithmic post-processing of several lower resolved images. It can increase the space-bandwidth product of an optical system by computationally combining images captured under different illumination conditions. Vignetting determines the spatial extent of the bright field and dark field regions in the captured images that contain information about low and high frequency image content, respectively. State-of-the-art analyses treat vignetting as a nuisance that needs to be reduced or excluded from algorithmic consideration by means of ad-hoc decision rules [1]. In contrast, this work investigates vignetting effects as a tool to infer a range of properties of the optical system. To achieve this, we characterize the individual system components of the experimental setup and compare experimental data to both, geometrical and wave optical simulations. We demonstrate that using vignetting as an analytical tool enables the modeling of the geometric and coherence properties of the optical system as evidenced by the good agreement between our simulation and experiment. Moreover, our work investigates pupil aberrations in the FPM setup and enables their partial characterization, despite not yet encompassing all aspects.

<http://dx.doi.org/10.1364/ao.XX.XXXXXX>

FPM is an innovative method for achieving highly resolved 2D and 3D reconstructions [2–4] with a wide spectrum of applications in industry and biological and medical fields [5–7]. This is due to its efficiency in obtaining a high spatial bandwidth beyond the diffraction limit of the objective lens formulated by Ernst Abbe [8]. The FPM setup comprises an LED array, an objective lens, a tube lens, and a camera sensor to record the captured images, as can be seen in Figure 1. By turning on one of the LEDs, it sends an electromagnetic field which interacts with the specimen placed in front of it and the exit field continues to propagate through the two lenses which magnify the image and a final image is recorded at the sensor plane. In conventional

microscope settings, with a constant space-bandwidth product, there is a trade-off between capturing high resolution information (high-NA) and a wide Field of View (FoV, low-NA setting). In contrast, FPM typically uses a low NA objective, capturing multiple low resolution, but wide FoV images. Algorithmic post-processing then computes high-resolution, wide-FoV images, i.e. the space-bandwidth product is increased beyond that of the physical system. High-quality reconstructions require the knowledge of 1) first-order geometrical properties, 2) coherence properties, and 3) aberrations of the optical system [9]. Usually, this knowledge is inferred via additional optimization goals in the FPM reconstruction procedure [3]. Since the resulting optimization problem is non-linear and non-convex, it is, however, uncertain whether accurate values are being recovered using this process.

In this work, we therefore aim at identifying system properties that can be inferred from direct observation. For this, we adopt a novel perspective on vignetting as a characteristic property of the optical system that is easily accessible and that carries valuable information about the system that can be extracted by careful analysis. We show that the geometric properties of a system (1) and its coherence properties (2) can be characterized to an accuracy as to enable predictive simulation, see for example Fig. 3. Moreover, we demonstrate that the presence of 4D aberrations can be effectively detected, yet, further studies are required for a precise system calibration. In addition, vignetting can be used for a suitable alignment of the optical system as we show later.

For the purposes of this letter, we analyze an FPM setup that was constructed in our lab. The illumination unit in the experimental setup employs a programmable Adafruit 32x32 LED array, where each LED is controlled using an Arduino microcontroller to emit (R,G,B) light with a spacing of 4mm between each LED. The setup uses a 10x 0.3NA Nikon objective lens, combined with a 200mm focal length, infinity-corrected tube lens (Thorlabs TTL 200). We use a consumer-grade camera (Canon 5D mark II) due to its large sensor area as well as a high resolution of $5,634 \times 3,753$ pixels with a pixel size of $6.4\mu\text{m}$. We capture images of the NBS 1963A Pattern using the (R,G,B) modes of the LEDs. The camera's large sensor is able to capture almost the full extent of the unvignetted area, visible as a circle containing the object.

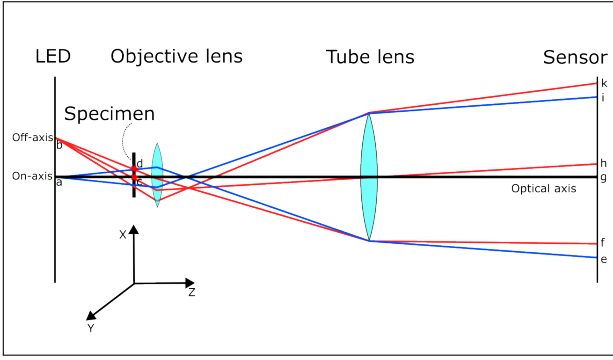


Fig. 1. A ray diagram of the FPM setup with X-Y planes representing the LED illumination, specimen, objective lens, tube lens and sensor. The coordinate system of the setup is also displayed. The blue and red rays correspond to the on-axis and off-axis cases, respectively. Image regions within a cone of light are referred to as bright field, whereas regions outside of it are dark field regions.

Alignment. A first advantage of studying vignetting lies in its usefulness for a suitable alignment of the optical system, see Fig. 2. If the sensor is chosen to be sufficiently large, a bright circle becomes visible in the image plane, separating bright field and dark field regions, see Fig. 1. In our setup, this vignetting circle (VC) is caused by the tube lens restricting the propagation of light for on- and near-axis LEDs. Assuming a sensor centered on the optical axis, e.g. with the aid of an alignment laser, the LED array can be centered by moving its center LED such that the vignetting circle is centered on the sensor. This is best done with live view capabilities. For further system alignment, it is useful to activate several LEDs, e.g. in an “L” or cross pattern, see Fig. 2 (top right), since the orientation of the LED array with respect to the sensor axis becomes visible and can be adjusted accordingly. In addition, an out-of-plane tilt in the LED array manifests as a change in the VC’s radius (bottom right). A second observation is that focusing the microscope with single LED illumination is difficult due to the near-coherent illumination and the corresponding effectively small NA, causing a very large depth of field. Activating multiple LEDs leads to the superposition of several specimen images (illustrated by the “A” pattern and assuming it to be planar) when the specimen is out of focus. Adjusting the focus shifts these copies w.r.t. each other (top left). Therefore, a good focus setting is achieved when the multiple images align on top of each other. For 3D samples, a suitable sample plane should be chosen as the reference focus in this manner. In both the 2D and 3D cases, a larger lateral LED distance from the center leads to increased sensitivity. A sensor tilt is visible as an elliptical shape of the VC, Fig. 2 (bottom left).

Geometric Characterization. In the following, we aim to match a simulation to observed intensity images of the vignetting circle. In a first step, we exploit, as a second property of the vignetting circle, its sensitivity to the construction parameters of the optical system. In particular, with reference to Fig. 1, the diameter $d_{VC} = \bar{e}i$ and relative displacement $M_{LED} = \bar{g}h/\bar{a}b$ of the vignetting circle add additional information over and above the standard object magnification M_{Obj} which is measured using a calibration target.

We formulate the determination of the optimal system parameters as an optimization problem: Given experimental values of

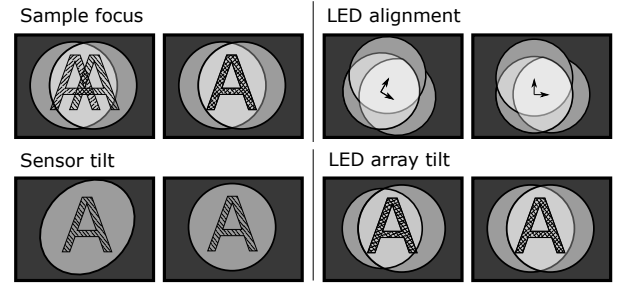


Fig. 2. Focusing (top left) and alignment (top right) can be finely adjusted activating multiple LEDs. Sensor and LED array tilt affect the eccentricity and relative scale of the VCs.

the three observables, d_{VC} , M_{LED} and M_{Obj} , determine the most likely construction parameters of the system, i.e. the axial distances, component diameters, focal lengths, pupil and principal plane positions as well as lateral LED spacing. Collecting the geometrical observables in a vector ϕ_g and the system parameters in a vector θ_g , and denoting a first-order ray optical simulation that is predicting the observables as $f_{geom}(\theta_g)$, we may write

$$\theta_g^* = \underset{\theta_g}{\operatorname{argmin}} \left\| f_{geom}(\theta_g) - \phi_g \right\|_2^2, \quad (1)$$

where θ_g^* is the vector of geometric system parameters causing the best fit between simulation and measurement. We initialize the optimization with the measured parameters θ_{g0} , with an estimate of their standard deviations. We then perform a Monte-Carlo (MC) sampling in the vicinity of the initial guess θ_{g0} , assuming independent Gaussian errors of the individual measurements to avoid local minima that may occur in our over-parameterized system, select the minimum and iteratively repeat the process with decreased standard deviation values. We did not observe multiple minima within the measurement uncertainties which suggests that a gradient descent optimization may be used in the future. Using the optimized parameters θ_g^* , we obtain a good agreement between the measurements and the simulations in all color channels as can be seen in Tab. 1. Furthermore, such parameters are input to the next step, a fitting of the coherence properties of the system.

Channel	Type	d_{VC} [mm]	M_{Obj}	M_{LED}
R/G/B	Sim.	34.20 (all)	9.96 (all)	0.32 (all)
	Meas.	33.89/33.97/33.99	10.16 (all)	0.31/0.31/0.30

Table 1. Comparison of the VC diameter and object and LED magnifications between simulations and measurements for the R, G and B channels.

Wave-Optical Characterization. Given the geometric properties of the optical system, we upgrade the simulation to the scalar wave regime in order to match the coherence properties of the system between simulation and measurement. The apertures in the system give rise to prominent diffraction patterns at the edges of the vignetting circle, the detailed structure of which is related to a) the geometric system parameters, most notably the aperture size and the propagation distance to the sensor,

and b) the coherence properties of the light source. We exploit this property by analyzing the diffraction pattern for the center LED in terms of the light source properties, see Fig. 3, and a refinement of the geometric system parameters, to establish the coherence properties of our FPM system.

We measure both the LED spatial emission profile and its emission spectrum for each color channel, respectively, by conducting a fit with a Gaussian function to extract the associated means and standard deviations μ_s, σ_s (spectral) and μ_x, σ_x (spatial), where μ_s, σ_s, μ_x and σ_x are determined for each of the (R,G,B) color channels. We capture images using all three illuminations, see Fig. 4 (top) and extract an intensity profile along the edge of the VC for each color channel using image processing: We detect the intensity maxima along the edge profile, generating a set of points, which we fit with an ellipse (we observe the geometrical shape to be elliptical indicating a sensor tilt, see bottom left of Fig. 2), establishing its midpoint and its major and minor axes. By varying the major and minor axes by a common scale factor, we can generate ellipses that are offset to the inside or outside of the ellipse approximating the intensity maxima. By averaging across the circumference of each ellipse, we extract a noise-reduced intensity value for each scale factor, resulting in the intensity profiles labeled "Experiment" in Fig. 3.

For simulation, we use the angular spectrum method, as described by Matsushima et al. [10], to accurately model wave field propagation, which implements Rayleigh-Sommerfeld diffraction theory without approximation. To simulate the partial coherence of the LED sources, we perform a MC sampling of the spatial ($\mu_x = 0, \sigma_x$) and spectral probability distributions (μ_s, σ_s) determined by our measurements, where μ_x, σ_x, μ_s , and σ_s are individually treated for the (R,G,B) color channels. We simulate 1000 coherent fields with uniformly distributed random initial phases that are superposed incoherently. The individual simulations are initialized with spherical wavefronts in the object plane and propagated through the system, treating the microscope objective and the tube lens as thin lenses with a perfect lens phase profile that maps a divergent spherical wave from the point source to a spherical wave converging to its Gaussian image point. For first order properties of the system, we use the optimized geometric system parameters θ_g^* . The simulation results in an intensity profile similar to the one labeled "Simulation" in Fig. 3, but generally not fitting the experimental curve precisely.

We therefore resort to another optimization to fit the intensity profiles. We vary the light source system parameters $\theta_c = (\mu_s^r, \sigma_s^r, \sigma_x^r, \mu_s^g, \sigma_s^g, \sigma_x^g, \mu_s^b, \sigma_s^b, \sigma_x^b)$, where the superscripts indicate the respective values for the color channels. Moreover, we adjust the θ_g^* geometric parameters using a new variable $\hat{\theta}_g$, while keeping it close to the previous result θ_g^* . Due to the wavy nature of the intensity profiles and the sensitivity of the curve to the light source parameters it is not advisable to compare the curves directly. Instead, we opt for comparing the positions of the first four local intensity maxima (as seen from the edge) of the profiles, Fig. 3, collecting them in an observable vector ϕ_c . Denoting the wave optical simulation and subsequent peak fitting as $f_{wave}(\theta_c; \theta_g)$, we formulate the optimization as

$$\theta_c^*, \hat{\theta}_g^* = \underset{\theta_c, \hat{\theta}_g}{\operatorname{argmin}} \|f_{wave}(\theta_c; \hat{\theta}_g) - \phi_c\|_{2,1} + \lambda \|\hat{\theta}_g - \theta_g^*\|_2^2, \quad (2)$$

where the group L2-norm is taken per local intensity maximum. The standard deviation in the geometric parameters is iteratively reduced during optimization. The final fit is shown in Fig. 3,

denoted as simulation. Note that the result uses a single set of geometric system parameters $\hat{\theta}_g^*$, whereas the light sources use the respective θ_c^* . We have therefore obtained a single system description that can predictively simulate the diffraction behavior of our system at different wavelengths, as can be seen in Fig. 3.

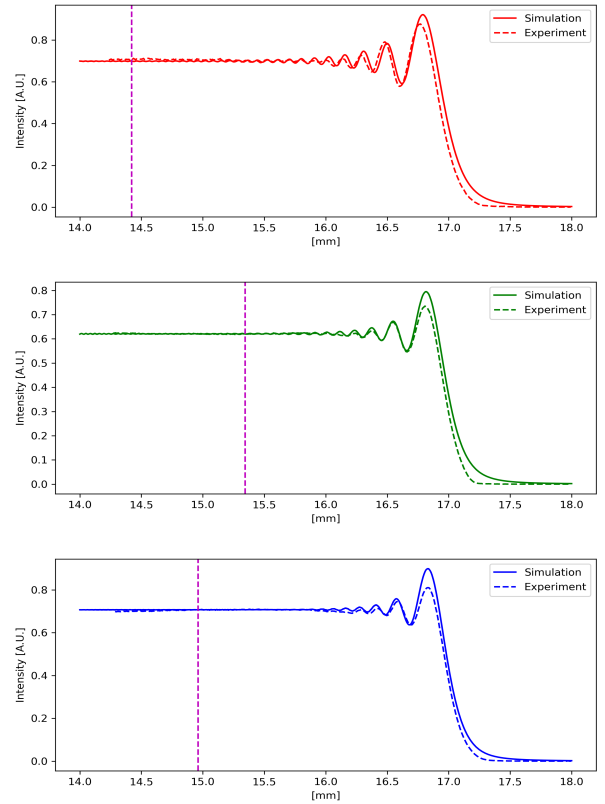


Fig. 3. VC's profile of the measurements (dashed line) is overlaid to 1D simulation (solid line) for the R, G, and B channels (top to bottom). The vertical lines are the temporal coherence length of the respective wavelength. Notice the peaks extending to the left cease prior to the temporal coherence length due to the influence of the spatial coherence.

Aberrations. In a perfectly aligned system, the center LED creates a virtual point source on the optical axis, illuminating a centered exit pupil orthogonal to the optical axis, creating a circular image on a sensor, which is also positioned orthogonally to the axis. Provided that LEDs form a regular grid, also placed orthogonal to the axis, illuminating the specimen individually, a similar grid of circles, of equal sizes, should be observed on the image plane.

Experimentally, we instead observe varying elliptical shapes of the vignetting circle, Fig. 4, with non-linear translations as evidenced by their centers plotted in Fig. 5 (a) w.r.t. different LED positions. In the following, we aim to explain this discrepancy.

We observe an elliptical shape of the vignetting circle for the center LED. This shape can be explained by a sensor tilt as the circular cone generated by the virtual point source is intersected by a tilted plane, resulting in the observed ellipse. Its minor axis corresponds to the tilt axis, whereas its eccentricity is related to the tilt angle. Notably, a tilt in the LED plane will not cause an elliptical shape as long as the exit pupil is circular and parallel to the sensor plane.

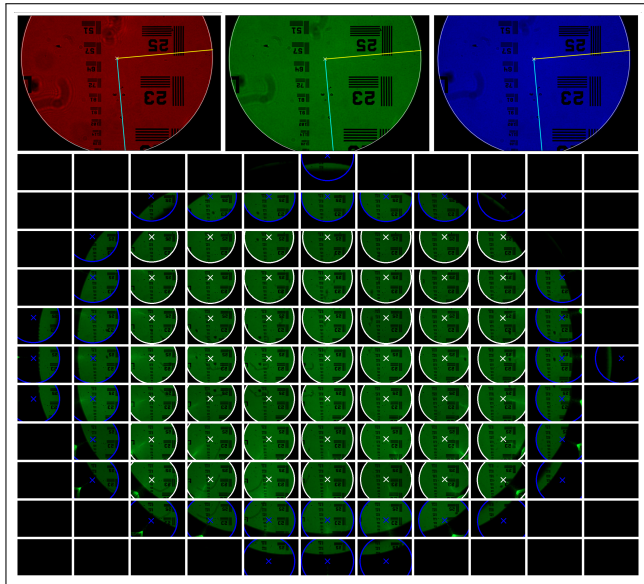


Fig. 4. Grid of images of the NBS 1963A Pattern illuminated by green LEDs and fitted to ellipses. Elliptical contours resulting from the VC fits are superimposed on the individual images in white/blue. The top row shows the images of the on-axis LED in (R,G,B), where the yellow and cyan lines represent the minor and major semi-axes, respectively.

To first order, an off-axis change of the LED position leads to a linear change in the length of the ellipse axes, while their orientation remains constant. We validated that our system parameters θ_g^* , are in this linear range. Due to the observations in the previous paragraph, we expect this component to be present in our system. In order to validate this hypothesis, we individually fit ellipses to all accessible vignetting circles, Fig. 4 (bottom, white outlines), followed by a fit of a polynomial model in each of the ellipse parameters (center, axes, orientation) across LED field positions. This model is refined on partially visible vignetting circles, Fig. 4 (bottom, blue outlines). Since we validated a sensor tilt in the first step, we subtract the linear component of the ellipse's major and minor axes model, in Fig. 5 (c) and (d) to underscore the presence of higher order distortion terms in the optical system.

The shown residual components and the orientation field, Fig. 5 (b), of the ellipses form a preliminary probe into the aberration behavior of the optical system: Assuming that the ellipses result from a linear stretch of the image along their major and minor axes, we can relate this assumed geometric image distortion to a refocus term in the wavefront. The varying ellipse components, excluding tilt-induced changes, therefore indicate an LED field-varying astigmatism being present in the system. In practice, this results in a combination of blur and geometric distortion that should be compensated for optimal performance. We therefore recommend to use a full 4D aberration function to improve the reconstruction quality, however, it is beyond the scope of this work to demonstrate the expected effect.

The described LED-field varying predictive model has the additional benefit of being usable to predict bright- and dark-field regions in an image. For the full benefit, the vignetting caused by the objective lens (second, unfitted circular arc in Fig. 4 bottom) should also be incorporated.

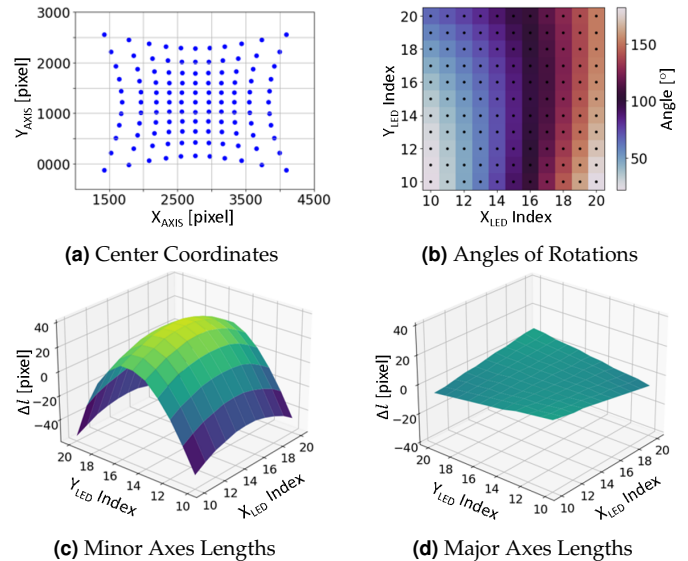


Fig. 5. Visualization of the vignetting model parameters. Each data point in the grid corresponds to one LED being active, the plots show the respective ellipse parameters. In (c) and (d), Δl represents the axes lengths subtracted from their corresponding linearizations.

Conclusions. In conclusion, we have investigated vignetting effects in FPM and identified them as a rich source of information about the underlying optical system. A primary benefit of examining vignetting is its critical role in optimizing the alignment of the optical system. Moreover, these effects not only allow us to determine the geometric construction parameters of the system, but also enable us to characterize the partial coherence properties necessary to predict interference effects faithfully in simulations. Furthermore, our analysis reveals that aberrations are evident in our setup, necessitating an advanced 4D treatment. We expect that this approach will yield substantial improvements in the reconstruction results.

Funding. German Research Foundation (DFG) under grants FOR 5336 (IH 114/2-1 and MO 2962/11-1).

Disclosures. The authors declare no conflicts of interest.

Data availability. Data underlying the results presented in this paper are not publicly available at this time but may be obtained from the authors upon reasonable request.

REFERENCES

1. A. Pan, Z. Chao, X. Yuege, L. Ming, and Y. Baoli, *Opt. Lasers Eng.* **120**, 40–48 (2019).
2. G. Zheng, R. Horstmeyer, and C. Yang, *Nat. Photonics* **7**, 739–745 (2013).
3. L. Tian, X. Li, K. Ramchandran, and L. Waller, *Biomed. Opt. Express* **5**, 2376 (2014).
4. L. Tian and L. Waller, *Optica* **2**, 104 (2015).
5. G. Zheng, C. Shen, S. Jiang, P. Song, and C. Yang, *Nat. Rev. Phys.* **3**, 207 (2021).
6. C. K. Pavan, L. Loetgering, K. C. Zhou, S. Xu, A. R. Harvey, and R. Horstmeyer, *Opt. Express* **28**, 9603 (2020).
7. A. Pan, C. Zuo, and B. Yao, *Reports on Prog. Phys.* **83**, 096101 (2020).
8. E. Abbe, *Arch. für Mikroskopische Anat.* **9**, 413 (1873).
9. L.-H. Yeh, J. Dong, J. Zhong, L. Tian, M. Chen, G. Tang, M. Soltanolkotabi, and L. Waller, *Opt. Express* **23**, 33214 (2015).
10. K. Matsushima and T. Shimobaba, *Opt. express* **17**, 19662 (2009).